Surface & Coatings Technology 513 (2025) 132535

Contents lists available at ScienceDirect

Surface & Coatings Technology

journal homepage: www.elsevier.com/locate/surfcoat

Investigation of nanocomposite formation in TiSiN coatings using atom probe tomography☆

Saeideh Naghdali [a], Maximilian Schiester [b,c], Velislava Terziyska [a], Marcus Hans [d], Daniel Primetzhofer [e], Markus Pohler [f], Christoph Czettl [f], Michael Tkadletz [c], Nina Schalk [a,b,*]

[a] Department of Materials Science, Montanuniversität Leoben, Franz Josef-Straße 18, 8700 Leoben, Austria
[b] Christian Doppler Laboratory for Advanced Coated Cutting Tools at the Department of Materials Science, Montanuniversität Leoben, Franz Josef-Straße 18, 8700 Leoben, Austria
[c] Christian Doppler Laboratory for Sustainable Hard Coatings at the Department of Materials Science, Montanuniversität Leoben, Franz Josef-Straße 18, 8700 Leoben, Austria
[d] Materials Chemistry, RWTH Aachen University, Kopernikusstraße 10, 52074 Aachen, Germany
[e] Department of Physics and Astronomy, Uppsala University, Lägerhyddsvägen 1, 75120 Uppsala, Sweden
[f] CERATIZIT Austria GmbH, Metallwerk-Plansee-Straße 71, 6600 Reutte, Austria

ARTICLE INFO

Keywords:
APT
Si variation
Isotopic substitution
Hard coatings
Microstructure

ABSTRACT

Owing to their superior mechanical properties, TiSiN nanocomposite coatings are known as excellent protective layers for cutting tools. In the present study, isotopic substitution of N is applied to investigate the nanostructure of TiSiN coatings with varying Si contents using atom probe tomography (APT). TiSiN coatings containing ~2, 5, and 10 at% Si were sputter-deposited using ^{15}N-enriched nitrogen. The APT results show that Si enriches at assumed grain boundaries forming an amorphous phase for all investigated coatings. This result is corroborated by complementary performed high resolution scanning transmission electron microscopy investigations. Further, no Si-free regions could be observed by APT, evidencing that for all coatings Si is also incorporated into a $Ti_{1-x}Si_xN$ solid solution. In addition, also no Ti-free regions are present, indicating that the amorphous phase can be assigned as a-$Si_aTi_bN_c$. With increasing the overall Si content from ~2 to 10 at% the Si incorporated into the solid solution increases from ~2 to ~9 at%, while the Si-enrichment in the amorphous phase fraction is rather constant at ~4 to 6 at%. The highest hardness of 38.5 ± 1.4 GPa, as determined by nanoindentation, was obtained for the coating containing ~5 at% Si. This study demonstrates that isotopic substitution of nitrogen is a suitable tool to study the nanocomposite structure of TiSiN coatings in unprecedented detail.

1. Introduction

In the last decades, Si has proven to be a suitable alloying element for TiN hard coatings used in cutting applications to improve the oxidation and wear resistance [1,2]. The addition of Si to TiN is commonly reported to result in the formation of nanocomposite TiSiN coatings, consisting of face-centered cubic (fcc) Ti(*Si*)N nano-crystals surrounded by an amorphous (a) SiN_x phase [3,4]. Adjusting the Si content in TiSiN nanocomposite coatings has been shown to result in varying hardness values (22–45 GPa) [5–7], highlighting the effect of the fraction and composition of the amorphous tissue phase on material properties [8]. It is reported that the a-SiN_x phase plays a grain refining role in nanocomposite coatings as it hinders grain growth and inhibits grain boundary sliding [9]. Vepřek et al. [3] claimed that TiSiN nanocomposite coatings reach a maximum hardness of ~50 GPa when the thickness of the amorphous tissue phase is 1–2 monolayers. However, the characterization of the nanostructure and particularly the accurate determination of the local elemental distribution of TiSiN coatings is quite challenging, due to the low thickness of the a-SiN_x and the close binding energies of crystalline and a-SiN_x in X-ray photoelectron spectroscopy [10,11]. Atom probe tomography (APT) is a suitable characterization technique for the investigation of the local elemental distribution of materials close to the atomic scale [12], but inherent limitations in resolving peak overlaps of Si and natural abundant

☆ This article is part of a Special issue entitled: 'Women in SCT' published in Surface & Coatings Technology.

* Corresponding author at: Department of Materials Science, Montanuniversität Leoben, Franz Josef-Straße 18, 8700 Leoben, Austria.
E-mail address: nina.schalk@unileoben.ac.at (N. Schalk).

https://doi.org/10.1016/j.surfcoat.2025.132535
Received 10 April 2025; Received in revised form 30 June 2025; Accepted 28 July 2025
Available online 29 July 2025

nitrogen in the mass spectrum complicate the evaluation of TiSiN [13]. Engberg et al. [14] succeeded to differentiate the peak overlaps of Si and N species by isotopic substitution of natural abundant nitrogen with ^{15}N. They observed nm-scale Si compositional fluctuations in cathodic arc deposited TiSiN coatings through voxelized APT data analysis and confirmed Si segregation at the nm-scale using TEM. Numerous publications reported on the formation of solid solution or nanocomposite structures in sputter-deposited TiSiN coatings [9,15–19]. However, APT has not been utilized in any of these studies. In our recent publication, we systematically investigated the capabilities of the isotopic substitution approach to enhance elemental and imaging accuracy, and spatial resolution in APT analyses of sputter deposited TiSiN coatings. By examining single layer and model multilayer coatings, we demonstrated that isotopic substitution can improve both, the elemental and imaging accuracy of APT measurements of TiSiN coatings [20]. The aim of this study is to investigate the effect of different Si contents on the formed nanostructure and local elemental distribution of TiSiN coatings using APT and the developed methodological approach of isotopic substitution. TiSiN coatings containing ~2, 5, and 10 at% Si were sputter deposited. The microstructure was studied by a combination of X-ray diffraction (XRD) and high-resolution scanning transmission electron microscopy (HR-STEM). Additional nanoindentation tests enabled a correlation of the microstructure with the mechanical properties.

2. Materials and methods

Reactive unbalanced d.c. magnetron sputter deposition of TiSiN coatings with aimed varying Si contents of 2, 5, and 10 at% (labelled in the following $TiSi_2N$, $TiSi_5N$, and $TiSi_{10}N$) was conducted on Si substrates with dimensions of 7 × 21 mm^2 in a mixed Ar/N_2 atmosphere. The deposition system was equipped with one solid Ti target (99.995 %, Ø 2 in) and one solid Si target (99.990 %, Ø 2 in). The substrate holder was positioned at a distance of 45 mm from the targets. The substrate temperature was 700 °C, the bias voltage was set to −50 V, and the Ar and N_2 partial pressures were 0.38 and 0.04 Pa, respectively. A ^{15}N-enriched gas containing 98 at% ^{15}N was used in this study, which was purchased from Sigma-Aldrich. The Si content in the coatings was varied by adjusting the target currents. The respective target currents are summarized in Table 1 as well as the reference compositions of the coatings, which were determined by complementary ion beam based techniques utilizing the 5 MV Pelletron tandem accelerator at the Tandem Laboratory of Uppsala University [21]. Elastic recoil detection analysis (ERDA) using 36 MeV I^{8+} primary ions and Rutherford backscattering spectrometry (RBS) using 2 MeV He^+ primary ions were employed, and a stoichiometric TiN reference sample was used [22]. The obtained compositions are in fair agreement with the aimed values and the sum of O and Ar impurities were < 2 at%. The thicknesses of the coatings, which are also given in Table 1, were determined from focused ion beam (FIB) prepared cross-sections using a field emission scanning electron microscope from Zeiss (Crossbeam 550).

The structure of the coatings was studied using a Bruker D8 Advance X-ray diffractometer equipped with Cu-Kα radiation using offset coupled θ/2θ scans with an offset of 2° to avoid influence of the substrate. Diffractograms were captured within a range of 20 to 85°, utilizing a step size of 0.01° and a measurement duration of 1 s per step. In addition, the residual stresses were determined using wafer curvature measurements utilizing the reflection of two parallel laser beams (distance: 15 mm) provided by a He—Ne laser (λ = 632.8 nm), to determine the curvature radius of the samples [23,24].

The specimens for the APT measurements were prepared via the standard lift-out technique [25] and subsequent sharpening by annular FIB milling, applying the already mentioned Crossbeam 550 from Zeiss. The specimens were analyzed in laser-assisted mode, utilizing a CAMECA LEAP 5000 XR atom probe, equipped with an ultraviolet laser (wavelength of 355 nm). A laser pulse energy of 30 pJ was employed. The laser pulse frequency, base temperature, and detection rate were maintained at 250 kHz, 50 K, and 0.5 %, respectively. Data analysis was performed using the IVAS module embedded in the AP Suite 6.3 software package by CAMECA. To gain additional insights into the microstructure HR-STEM investigations were conducted exemplarily on the $TiSi_5N$ coating. The lamella was prepared using FIB (FEI Nova200) milling. HR-STEM was conducted on a probe corrected FEI Titan 3 G2 60–300 (S/TEM) microscope, equipped with an X-FEG Schottky field-emission electron source operated at 300 kV (current of 150 pA, beam diameter of 1 Å). The spectrum images were captured with an FEI Super-X detector (Chemi-STEM technology), which includes four separate silicon drift detectors.

The hardness and Young's modulus of the TiSiN coatings were assessed through nanoindentation, employing a KLA G200 nanoindenter, equipped with a diamond Berkovich tip (Synton-MDP). A constant indentation strain-rate of 0.05 s^{-1} was applied up to an indentation depth of 500 nm. Continuous stiffness measurements (CSM) were performed with a 2 nm harmonic displacement at 45 Hz, enabling continuous assessment of Young's modulus and hardness. Data were analyzed using the Oliver and Pharr [26] method with a Poisson's ratio of 0.24 for TiSiN as well as a Poisson's ratio of 0.07 and Young's modulus of 1141 GPa for the diamond tip. Results were averaged over an indentation depth of 70–150 nm, following the 10 % rule [27].

Table 1
Target currents, elemental composition and thickness of TiSiN coatings.

Coating ID	Target current [A]		Elemental composition by ERDA/RBS [at%]			Thickness [μm]
	Si	Ti	Ti	Si	N	
$TiSi_2N$	0.01	0.45	47.1 ± 1.5	2.3 ± 0.1	50.6 ± 1.5	~1.9
$TiSi_5N$	0.02	0.40	45.1 ± 1.4	4.3 ± 0.1	50.6 ± 1.5	~1.7
$TiSi_{10}N$	0.04	0.35	38.7 ± 1.2	9.7 ± 0.3	51.6 ± 1.6	~1.5

3. Results and discussion

Fig. 1 shows the X-ray diffractograms of the TiSiN coatings with different Si contents of 2, 5, and 10 at%. All coatings exhibit peaks of fcc-TiN (the reference peak positions are added with dashed lines; [28]). In addition, Si peaks can be observed which most probably stem from the Si substrate, however, it cannot be completely excluded that they originate from excess elemental Si within the coating. No further peaks related to Si-containing compounds are present. The dominant fcc-TiN (111) peak for the coatings with 2 and 5 at% Si indicates that TiSiN with low Si content exhibits a preferred orientation towards (111). Increasing Si to 10 at% results in a less pronounced texture. It could be speculated that at higher Si contents the amorphous phase fraction increases, resulting in continuous recrystallization and grain refinement and consequently a more random texture [11,29]. With increasing Si content, a peak broadening can be observed, which implies a decreasing grain size and/or increasing microstrain [30]. Further, the peak positions are slightly shifted to lower angles as the Si content increases. The incorporation of Si into the TiN lattice results in a decrease of the lattice parameter and thus in a peak shift to higher diffraction angles [31], while the presence of compressive stress in the coating which is also commonly reported for TiSiN [6,9,30,32] results in a peak shift to lower angles. The presence of compressive residual stresses could be confirmed by wafer curvature measurements. Increasing of the Si content from 2 to 5 at% results in a significant increase of the residual stress from −5481 to −8396 MPa, while a further increase of the Si content to 10 at% leads to a decrease of the stress to −5709 MPa. A similar stress evolution with increasing Si content was also reported by Martin and Bendavid [7] and Cheng et al. [5].

In order to investigate the local elemental distribution with high resolution, APT was employed. The mass spectra of the TiSiN coatings containing ~20 million ions can be found in Fig. S1, in the Supplementary material. They exhibit peaks related to the expected elemental

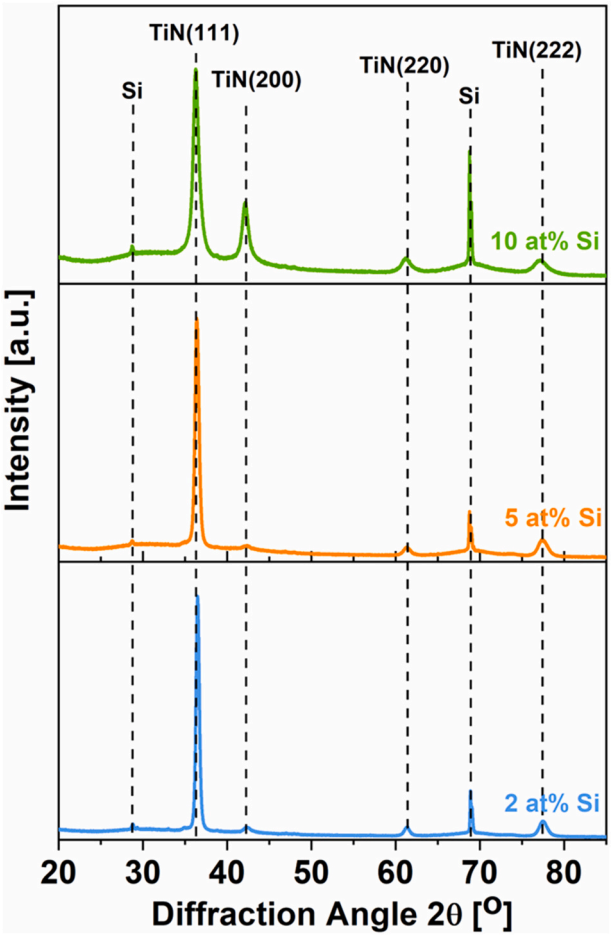

Fig. 1. X-ray diffractograms of TiSiN coatings with different Si contents.

species (Si^+, Si^{2+}, N^+, Ti^{2+}, Ti^{3+}), their corresponding molecular ions (N_2^+, TiN^{2+}, Ti_2N^{3+}, SiN^+) as well as Ar, O and C peaks. Peak overlaps of Si and N ion species at mass-to-charge state ratios of 14, 15, 28, 29, and 30 Da, which occur when natural abundant nitrogen is used in the deposition process, have been reduced to minimum by employing substituted nitrogen during deposition [14,20]. Based on isotopic ratios, the peaks at 14, 14.5, and 28 Da are attributed to $^{28}Si^{2+}$, $^{29}Si^{2+}$, and $^{28}Si^+$, respectively, while those at 15, 29, and 30 Da are assigned to $^{15}N^+$, $^{14}N^{15}N^+$, and $^{15}N_2^+$, respectively. Additional details about detected ion species and related mass-to-charge state ratios are provided in Table S1, in the Supplementary material. Fig. 2a presents a detailed APT analysis of the $TiSi_2N$ coating, where isoconcentration surfaces are used to visualize Si- and Ti-enriched regions. The reconstruction reveals an elongated microstructure in the growth direction of the $TiSi_2N$ coating, where Si-enriched areas can be distinguished from Ti-enriched regions. Considering the X-ray diffractograms in Fig. 1, the Ti-enriched areas can be assigned to the fcc-TiN-based structure, while the Si-enriched areas can be attributed to the formation of an amorphous phase fraction at assumed grain boundaries, providing evidence for a nanocomposite structure. The 1D compositional profile shown in Fig. 2b, corresponding to the region of interest (ROI) marked in the overlay of Si and Ti iso-concentration surfaces in Fig. 2a, further corroborates the presence of Si-enriched regions separating Ti-enriched areas with only minor Si-contents <2 at%. However, there are neither Si- nor Ti-free regions, confirming the formation of an fcc-$Ti_{1-x}Si_xN$ solid solution rather than a Si-free fcc-TiN phase [9,15]. In addition, the presence of Ti in Si-enriched regions indicates that the amorphous phase is a-$Si_aTi_bN_c$. This result is in contrast to the majority of literature on nanocomposite TiSiN coatings in general, but also specifically for sputter deposited coatings, where the amorphous phase is typically either specified as Si_3N_4 [3,33–35] or as SiN_x [9,15–18,36–38]. None of these studies applied APT, though. Therefore, introducing isotopic substitution of N, Engberg et al. [14] could show nm-scale segregations in cathodic arc deposited TiSiN coatings. Adapting this approach for sputter deposited TiSiN coatings [20] allows us now to evaluate their nanostructure in unprecedented detail.

Similar to the $TiSi_2N$ coating, the iso-concentration surfaces of the

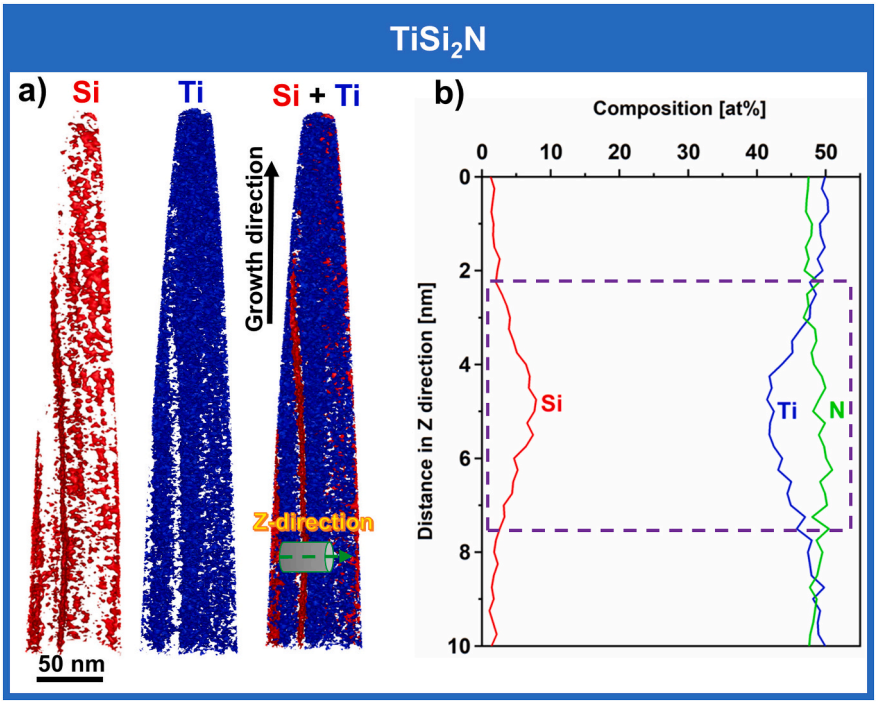

Fig. 2. a) 3D-reconstruction showing an Si iso-concentration surface (red) of 5.0 at%, an Ti iso-concentration surface of 50.1 at% (blue) and a combination of Si and Ti iso-concentration surfaces, where the ROI is marked. b) 1D compositional profile corresponding to the ROI marked in a).

$TiSi_5N$ coating in Fig. 3a show an elongated microstructure, with Si-enriched regions, separating Ti-enriched regions. The 1D compositional profile shown in Fig. 3b, corresponding to the ROI marked in the Si + Ti isoconcentration surface in Fig. 3a, further corroborates that there are neither Si-free nor Ti-free areas. Moreover, the 1D compositional profile shows that with increasing overall Si content to 5 at%, also more Si is present in the Ti-enriched regions, implying that more Si is incorporated into the $Ti_{1-x}Si_xN$ solid solution. The Si-enrichment (difference between content in the solid solution and maximum) in the amorphous phase fraction is with ~4 at% for the $TiSi_5N$ even lower than for the $TiSi_2N$ (~6 at%), albeit these absolute values should be viewed with caution considering the small investigated volume.

To get further information about the microstructure, the $TiSi_5N$ coating was exemplarily also investigated by HR-STEM. The overview of the cross-section of the lamella, shown in Fig. 4a, reveals a fine-grained structure with elongated grains, which is in excellent agreement with the APT results. Taking a closer look at higher magnification in Fig. 4b, it appears that crystalline regions (marked with green box), as also evidenced by the corresponding fast Fourier Transformation (FFT), are separated by a more disordered region. In Fig. 4c, along with the corresponding FFTs, the area marked with a red box is clearly crystalline, while the area marked with a blue box appears disordered. However, since the lamella was not ultimately thin, overlaps might also play a role here and it cannot be unambiguously concluded that these regions appearing disordered are really amorphous. Nevertheless, the energy dispersive X-ray spectroscopy (EDS) maps in Fig. 4d clearly show areas which are crystalline Si-enriched and simultaneously depleted in Ti, which is in excellent agreement with the APT results. Thus, the combination of XRD, TEM and APT results corroborates the formation of a fcc-$Ti_{1-x}Si_xN$/a-$Si_aTi_bN_c$ nanocomposite structure in the $TiSi_5N$ coating.

When the Si content is further increased to 10 at%, the elongated microstructure is maintained. The Si- and Ti-enriched regions can be also seen in Fig. 5a. Comparing the 1D compositional profiles displayed in Figs. 2b, 3b and 5b shows that increasing the overall Si content results in an increase of Si incorporated into the $Ti_{1-x}Si_xN$ solid solution from ~2 at%, via ~4 at% to ~9 at% for $TiSi_2N$, $TiSi_5N$ and $TiSi_{10}N$, respectively, while the Si-enrichment in the amorphous phase fraction is with ~6, 4 and again 6 at%, respectively, rather comparable for all three coatings. The relative Si-enrichment related to the Si content in the solid solution shows with 430, 100 and 70 % (rounded to full tens) for $TiSi_2N$, $TiSi_5N$ and $TiSi_{10}N$, respectively, a distinct trend, though. According to literature, sufficient thermal and/or kinetic activation is necessary for Si to segregate [4,9,39,40], While a rather high substrate temperature of 700 °C was applied in the present study, the bias voltage of −50 V was only moderate. Further, apart from the target currents to achieve an increasing Si content, the deposition conditions were held constant for the three investigated coatings. Thus, it could be argued that the constant deposition conditions result in comparable energetic growth conditions and consequently, in comparable mobility of Si during growth, which leads to an increasing Si content incorporated into the solid solution, while the enrichment in the amorphous phase fraction is rather constant [4]. The more pronounced incorporation of Si into the $Ti_{1-x}Si_xN$ solid solution with increasing overall Si content is also consistent with the observed peak broadening in XRD, since the incorporation of Si can be assumed to result in increased micro-strain. In addition, it could be speculated from the 3D-reconstructions in Figs. 2a, 3a, and 5a that the $Ti_{1-x}Si_xN$ grain size (blue regions) slightly decreases with increasing Si content, which also contributes to the peak broadening in XRD and reflects the chemical driving force of the increasing Si content.

In order to correlate the observed nanostructure with mechanical properties, nanoindentation was conducted. In Fig. 6, hardness as well as Young's modulus of the three investigated coatings are summarized. Compared to literature values for TiN, which are usually well below 30 GPa [1,37,41], the addition of only 2 at% Si results already in a significantly increased hardness of 35.9 ± 1.9 GPa. In general, the formation of a nanocomposite structure is reported to result in a higher hardness due to a reduced grain size and suppressed grain boundary sliding [40,42]. Increasing the Si content to ~5 at% results in a further hardness increase to 38.5 ± 1.4 GPa, which can most probably be related to an even smaller grain size and higher compressive residual stress (−8396 MPa). Adding 10 at% Si leads to a drop in hardness to 32.0 ± 1.9 GPa, which can be attributed to the increasing amorphous phase fraction formed at assumed grain boundaries with further decreasing grain size and also the lower observed compressive residual stress (−5709 MPa)

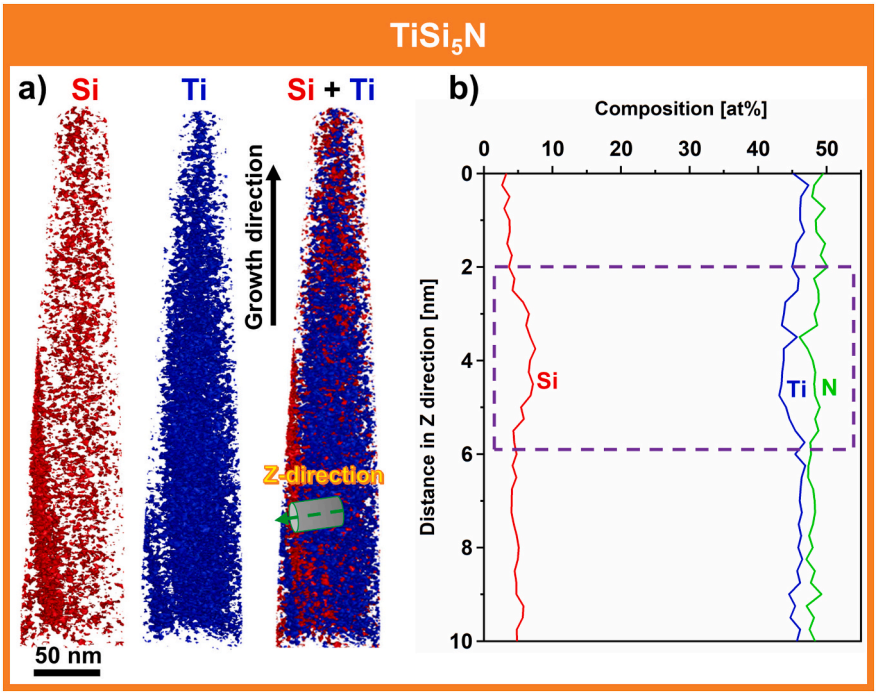

Fig. 3. a) 3D-reconstruction showing an Si iso-concentration surface (red) of 3.0 at%, an Ti iso-concentration surface of 43.0 at% (blue) and a combination of Si and Ti iso-concentration surfaces, where the ROI is marked. b) 1D compositional profile corresponding to the ROI marked in a).

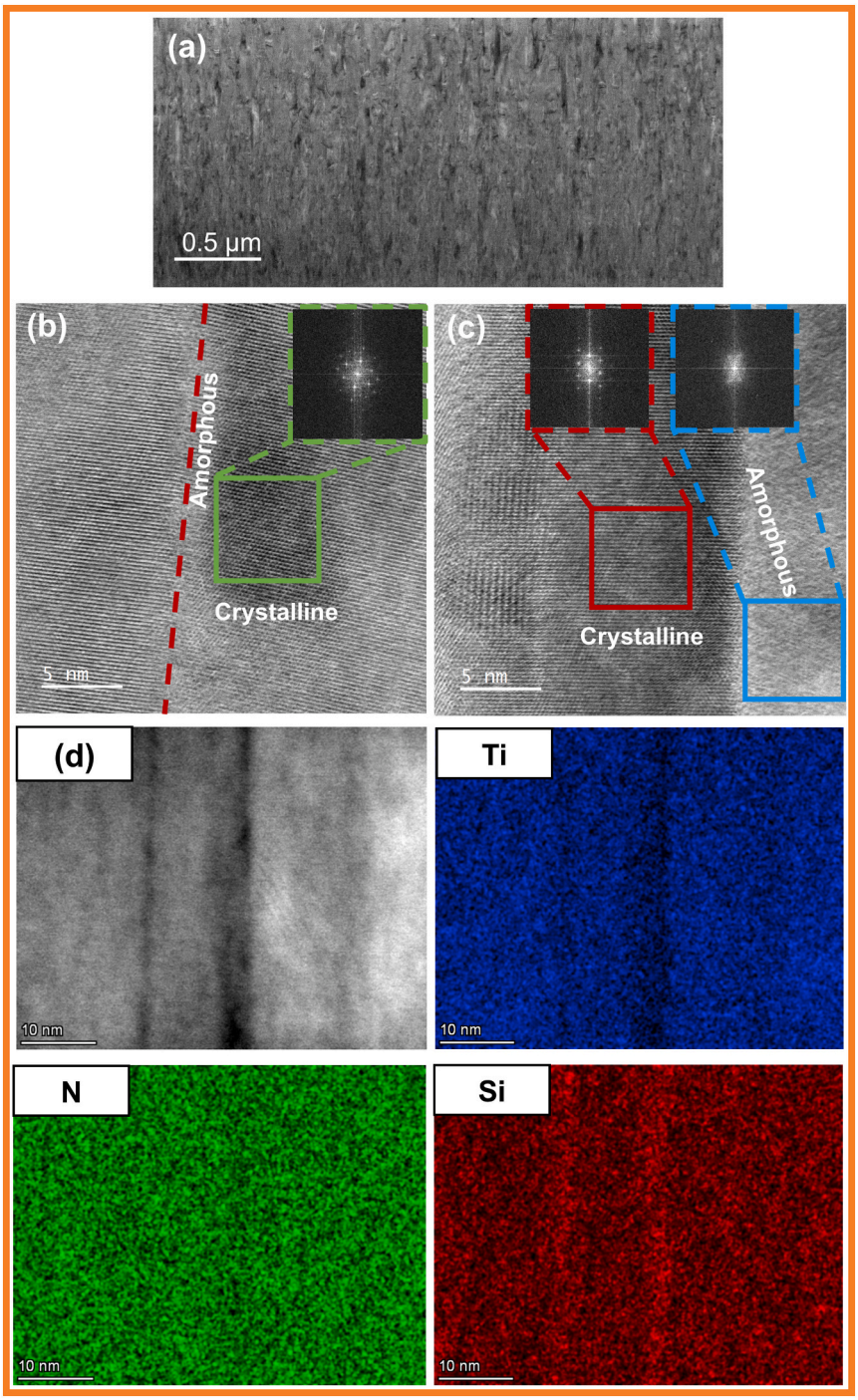

Fig. 4. a) STEM cross-sectional overview of a lamella of the $TiSi_5N$ coating, showing a fine-grained columnar structure. b) and c) HR- STEM images revealing elongated crystalline and amorphous regions with corresponding fast Fourier transformation of 5 × 5 nm regions, indicated with green, red and blue boxes. d) Detail of the microstructure with the corresponding energy dispersive X-ray spectroscopy maps revealing Si-enriched and Ti-depleted regions.

[43,44]. The observed hardness evolution is in good agreement with literature [9,15,45]. The evolution of the Young's modulus differs from the hardness, since it continuously decreases with increasing Si content from 405 ± 12 to 332 ± 11 GPa, which is in a fair agreement with literature [17,46] and can most probably be related to the decreasing grain size and thus, increasing amorphous phase fraction with increasing Si content [45–47].

4. Conclusions

Within this study the effect of different Si contents on the microstructure and the local elemental composition of TiSiN coatings was investigated in detail using atom probe tomography (APT) and isotopic substitution of N. Coatings with ~2, 5 and 10 at% Si were sputter deposited using ^{15}N-enriched nitrogen. The APT analysis revealed an elongated microstructure in growth direction, where larger Ti-enriched regions are separated by smaller Si-enriched areas. Further, neither Si- nor Ti-free regions could be observed. Since X-ray diffraction only

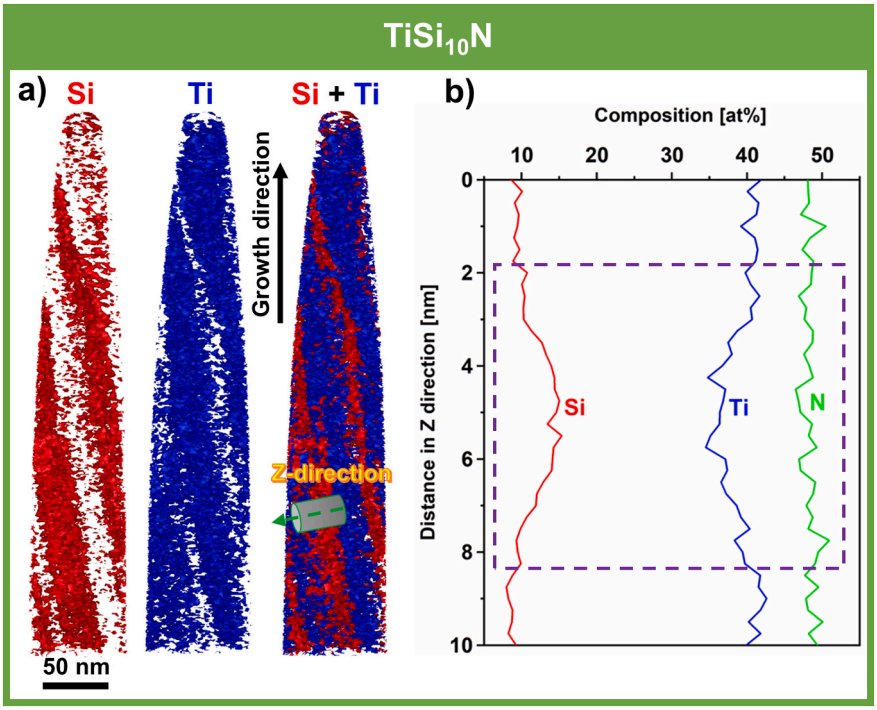

Fig. 5. a) 3D-reconstruction showing an Si iso-concentration surface (red) of 12.6 at%, an Ti iso-concentration surface of 41.6 at% (blue) and a combination of Si and Ti iso-concentration surfaces, where the ROI is marked. b) 1D compositional profile corresponding to the ROI marked in a).

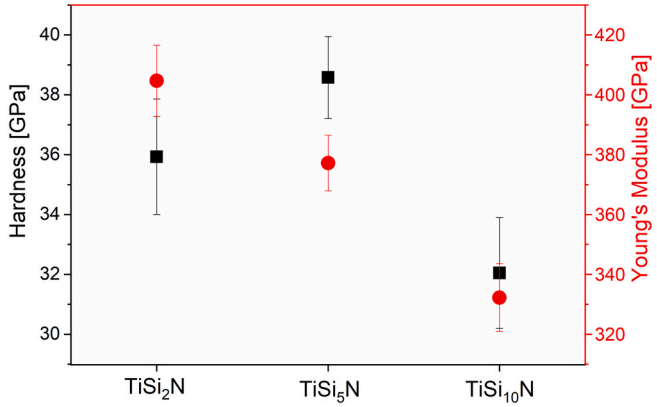

Fig. 6. Hardness and Young's modulus of TiSiN coatings.

provided evidence for the presence of face centered cubic (fcc)-TiN, the Ti-rich regions could be assigned as $Ti_{1-x}Si_xN$ solid solution, while the Si-rich regions could be assigned to the presence of an amorphous (a) $Si_aTi_bN_c$ phase, thus forming a fcc-$Ti_{1-x}Si_xN$/a-$Si_aTi_bN_c$ nanocomposite structure. With increasing overall Si content from 2 to 10 at%, the amount of Si incorporated into the solid solution increased from ~2 to 9 at%, while the Si-enrichment in the amorphous phase fraction stayed rather constant at ~4 to 6 at%. Complementary performed transmission electron microscopy and energy dispersive X-ray spectroscopy investigations corroborated the presence of larger crystalline regions, enriched in Ti and separated by smaller disordered Si-enriched areas. In addition, nanoindentation was conducted to correlate the microstructure with the mechanical properties of the studied TiSiN coatings. The maximum hardness of 38.5 ± 1.4 GPa was obtained for the coating containing ~5 at% Si. Further increase of the Si content to 10 at% resulted in a decreasing hardness, highlighting the influence of the amorphous phase fraction. Using isotopic substitution and APT, we were able to unveil the nanocomposite structure of sputter deposited TiSiN coatings in unprecedented detail. The applied methodology allows for a targeted design of the structure of TiSiN to optimize their performance.

CRediT authorship contribution statement

Saeideh Naghdali: Writing – original draft, Visualization, Validation, Methodology, Investigation, Formal analysis, Conceptualization. **Maximilian Schiester:** Writing – review & editing, Validation, Methodology, Investigation. **Velislava Terziyska:** Investigation, Formal analysis. **Marcus Hans:** Writing – review & editing, Investigation, Formal analysis. **Daniel Primetzhofer:** Writing – review & editing, Investigation, Formal analysis. **Markus Pohler:** Funding acquisition. **Christoph Czettl:** Funding acquisition. **Michael Tkadletz:** Writing – review & editing, Supervision, Methodology, Conceptualization. **Nina Schalk:** Writing – review & editing, Supervision, Project administration, Methodology, Funding acquisition, Conceptualization.

Declaration of Generative AI and AI-assisted technologies in the writing process

During the preparation of this work the authors used ChatGPT (openai.com) in order to enhance clarity and readability. After using this tool/service, the authors reviewed and edited the content as needed and take full responsibility for the content of the publication.

Declaration of competing interest

The authors declare that they have no known competing financial interests or personal relationships that could have appeared to influence the work reported in this paper.

Acknowledgements

The authors thank Konstantin Fischak and Bernhard Sartory from Materials Center Leoben for SEM/FIB work. Further, the authors want to thank Dipl. Ing. Magdalena Kirchmair for conducting the

nanoindentation experiments. The Austrian Research Promotion Agency (FFG) within the framework of the SEC^{3}T project (grant number: 896446) and the R&D infrastructure funding (Future Matter by APT, grant number: 884644) is gratefully acknowledged for financial support. Further, the financial support by the Austrian Federal Ministry of Labour and Economy, the National Foundation for Research, Technology and Development and the Christian Doppler Research Association is gratefully acknowledged. Accelerator operation at Uppsala University has been supported by the Swedish research council VR-RFI (#2019-00191).

Appendix A. Supplementary data

Supplementary data to this article can be found online at https://doi.org/10.1016/j.surfcoat.2025.132535.

Data availability

Data will be made available on request.

References

[1] L. Chen, Y. Du, S.Q. Wang, A.J. Wang, H.H. Xu, Mechanical properties and microstructural evolution of TiN coatings alloyed with Al and Si, Mater. Sci. Eng. A 502 (2009) 139–143, https://doi.org/10.1016/j.msea.2008.10.013.
[2] R. Akhter, Z. Zhou, Z. Xie, P. Munroe, TiN versus TiSiN coatings in indentation, scratch and wear setting, Appl. Surf. Sci. 563 (2021) 150356, https://doi.org/10.1016/J.APSUSC.2021.150356.
[3] S. Vepřek, S. Reiprich, A concept for the design of novel superhard coatings, Thin Solid Films 268 (1995) 64–71, https://doi.org/10.1016/0040-6090(95)06695-0.
[4] N. Schalk, Y. Moritz, G. Kumar, D. Holec, C. Hugenschmidt, V. Vadimovitch, L. Mathes, M. Schiester, C. Saringer, C. Czettl, M. Pohler, C. Mitterer, M. Tkadletz, Nanocomposite versus solid solution formation in the TiSiN system, Acta Mater. 275 (2024) 120063, https://doi.org/10.1016/J.ACTAMAT.2024.120063.
[5] Y.H. Cheng, T. Browne, B. Heckerman, P. Gannon, J.C. Jiang, E.I. Meletis, C. Bowman, V. Gorokhovsky, Influence of Si content on the structure and internal stress of the nanocomposite TiSiN coatings deposited by large area filtered arc deposition, J. Phys. D Appl. Phys. 42 (2009) 125415, https://doi.org/10.1088/0022-3727/42/12/125415.
[6] M. Nose, Y. Deguchi, T. Mae, E. Honbo, T. Nagae, K. Nogi, Influence of sputtering conditions on the structure and properties of Ti–Si–N thin films prepared by rf-reactive sputtering, Surf. Coat. Technol. 174-175 (2003) 261–265, https://doi.org/10.1016/S0257-8972(03)00710-2.
[7] P.J. Martin, A. Bendavid, Properties of $Ti_{1-x}Si_xN_y$ films deposited by concurrent cathodic arc evaporation and magnetron sputtering, Surf. Coat. Technol. 163-164 (2003) 245–250, https://doi.org/10.1016/S0257-8972(02)00491-7.
[8] X. Hu, H. Zhang, J. Dai, G. Li, M. Gu, Study on the superhardness mechanism of Ti–Si–N nanocomposite films: Influence of the thickness of the Si_3N_4 interfacial phase, J. Vac. Sci. Technol. A 23 (2005) 114–117, https://doi.org/10.1116/1.1821583.
[9] F. Vaz, L. Rebouta, P. Goudeau, J. Pacaud, H. Garem, J.P. Rivière, A. Cavaleiro, E. Alves, Characterisation of $Ti_{1-x}Si_xN_y$ nanocomposite films, Surf. Coat. Technol. 133–134 (2000) 307–313, https://doi.org/10.1016/S0257-8972(00)00947-6.
[10] H. Du, R.E. Tressler, K.E. Spear, C.G. Pantano, Oxidation studies of crystalline CVD silicon nitride, J. Electrochem. Soc. 136 (1989) 1527, https://doi.org/10.1149/1.2096955.
[11] F. Kauffmann, G. Dehm, V. Schier, A. Schattke, T. Beck, S. Lang, E. Arzt, Microstructural size effects on the hardness of nanocrystalline TiN/amorphous-SiN_x coatings prepared by magnetron sputtering, Thin Solid Films 473 (2005) 114–122, https://doi.org/10.1016/J.TSF.2004.08.080.
[12] B. Gault, A. Chiaramonti, O. Cojocaru-Mirédin, P. Stender, R. Dubosq, C. Freysoldt, S.K. Makineni, T. Li, M. Moody, J.M. Cairney, Atom probe tomography, Nat. Rev. Methods Primers 1 (2021) 51, https://doi.org/10.1038/s43586-021-00047-w.
[13] F. Tang, B. Gault, S.P. Ringer, P. Martin, A. Bendavid, J.M. Cairney, Microstructural investigation of Ti–Si–N hard coatings, Scr. Mater. 63 (2010) 192–195, https://doi.org/10.1016/J.SCRIPTAMAT.2010.03.050.
[14] D.L.J. Engberg, L.J.S. Johnson, J. Jensen, M. Thuvander, L. Hultman, Resolving mass spectral overlaps in atom probe tomography by isotopic substitutions – case of $TiSi^{15}N$, Ultramicroscopy 184 (2018) 51–60, https://doi.org/10.1016/J.ULTRAMIC.2017.08.004.
[15] M. Bartosik, R. Hahn, Z.L. Zhang, I. Ivanov, M. Arndt, P. Polcik, P.H. Mayrhofer, Fracture toughness of Ti-Si-N thin films, Int. J. Refract. Met. Hard Mater. 72 (2018) 78–82, https://doi.org/10.1016/J.IJRMHM.2017.12.015.
[16] M. Diserens, J. Patscheider, F. Lévy, Mechanical properties and oxidation resistance of nanocomposite TiN–SiN_x physical-vapor-deposited thin films, Surf. Coat. Technol. 120–121 (1999) 158–165, https://doi.org/10.1016/S0257-8972(99)00481-8.
[17] M. Diserens, J. Patscheider, F. Levy, Improving the properties of titanium nitride by incorporation of silicon, Surf. Coat. Technol. 108-109 (1998) 241–246, https://doi.org/10.1016/S0257-8972(98)00560-X.
[18] F. Vaz, L. Rebouta, B. Almeida, P. Goudeau, J. Pacaud, J.P. Riviere, J.B. e Sousa, Structural analysis of $Ti_{1-x}Si_xN_y$ nanocomposite films prepared by reactive magnetron sputtering, Surf. Coat. Technol. 120-121 (1999) 166–172, https://doi.org/10.1016/S0257-8972(99)00450-8.
[19] F. Vaz, P. Machado, L. Rebouta, J.A. Mendes, S. Lanceros-Méndez, L. Cunha, S.M. C. Nascimento, P. Goudeau, J.P. Rivière, E. Alves, A. Sidor, Physical and morphological characterization of reactively magnetron sputtered TiN films, Thin Solid Films 420–421 (2002) 421–428, https://doi.org/10.1016/S0040-6090(02)00812-X.
[20] S. Naghdali, M. Schiester, H. Waldl, V. Terziyska, M. Hans, D. Primetzhofer, N. Schalk, M. Tkadletz, Improving the elemental and imaging accuracy in atom probe tomography of (Ti,Si)N single and multilayer coatings using isotopic substitution of N, Ultramicroscopy (2025) 114200, https://doi.org/10.1016/J.ULTRAMIC.2025.114200.
[21] P. Ström, D. Primetzhofer, Ion beam tools for nondestructive in-situ and in-operando composition analysis and modification of materials at the Tandem Laboratory in Uppsala, J. Instrum. 17 (2022) P04011, https://doi.org/10.1088/1748-0221/17/04/P04011.
[22] M.A. Sortica, V. Paneta, B. Bruckner, S. Lohmann, M. Hans, T. Nyberg, P. Bauer, D. Primetzhofer, Electronic energy-loss mechanisms for H, He, and Ne in TiN, Phys. Rev. A 96 (2017) 032703, https://doi.org/10.1103/PHYSREVA.96.032703.
[23] C. Saringer, M. Tkadletz, C. Mitterer, Restrictions of stress measurements using the curvature method by thermally induced plastic deformation of silicon substrates, Surf. Coat. Technol. 274 (2015) 68–75, https://doi.org/10.1016/J.SURFCOAT.2015.04.038.
[24] G.G. Stoney, The tension of metallic films deposited by electrolysis, Proc. R. Soc. Lond. A. 82 (1909) 172–175, https://doi.org/10.1098/rspa.1909.0021.
[25] K. Thompson, D. Lawrence, D.J. Larson, J.D. Olson, T.F. Kelly, B. Gorman, In situ site-specific specimen preparation for atom probe tomography, Ultramicroscopy 107 (2007) 131–139, https://doi.org/10.1016/j.ultramic.2006.06.008.
[26] W.C. Oliver, G.M. Pharr, An improved technique for determining hardness and elastic modulus using load and displacement sensing indentation experiments, J. Mater. Res. 7 (1992) 1564–1583, https://doi.org/10.1557/JMR.1992.1564.
[27] S. Zak, C.O.W. Trost, P. Kreiml, M.J. Cordill, Accurate measurement of thin film mechanical properties using nanoindentation, J. Mater. Res. 37 (2022) 1373–1389, https://doi.org/10.1557/S43578-022-00541-1.
[28] Int. Cent. Diffr. Data, Pdf-2-Release, card number 00-038-1420.
[29] P.B. Barna, M. Adamik, Fundamental structure forming phenomena of polycrystalline films and the structure zone models, Thin Solid Films 317 (1998) 27–33, https://doi.org/10.1016/S0040-6090(97)00503-8.
[30] Y.X. Xu, L. Chen, Z.Q. Liu, F. Pei, Y. Du, Improving thermal stability of TiSiN nanocomposite coatings by multilayered epitaxial growth, Surf. Coat. Technol. 321 (2017) 180–185, https://doi.org/10.1016/J.SURFCOAT.2017.04.057.
[31] E. Mohammadpour, W.Y.H. Liew, N. Mondinos, M. Altarawneh, S. Lee, N. Radevski, M. Minakshi, A. Amri, H.N. Lim, Z.T. Jiang, Enhancement of thermal and mechanical stabilities of silicon doped titanium nitride coating by manipulation of sputtering conditions, J. Mater. Res. Technol. 17 (2022) 1122–1131, https://doi.org/10.1016/J.JMRT.2022.01.039.
[32] M.S. Ahmed, X. Zhao, Z. Zhou, P. Munroe, N. Chen-Tan, L.K.Y. Li, Z. Xie, Effect of thermal annealing upon residual stress and mechanical properties of nanostructured TiSiN coatings on steel substrates, J. Am. Ceram. Soc. 94 (2011) 1546–1551, https://doi.org/10.1111/j.1551-2916.2010.04280.x.
[33] S. Vepřek, M. Haussmann, S. Reiprich, L. Shizhi, J. Dian, Novel thermodynamically stable and oxidation resistant superhard coating materials, Surf. Coat. Technol. 86–87 (1996) 394–401, https://doi.org/10.1016/S0257-8972(96)02988-X.
[34] S. Vepřek, A. Niederhofer, K. Moto, T. Bolom, H.D. Männling, P. Nesladek, G. Dollinger, A. Bergmaier, Composition, nanostructure and origin of the ultrahardness in nc-TiN/a-Si_3N_4/a- and nc-$TiSi_2$ nanocomposites with HV=80 to ≥105 GPa, Surf. Coat. Technol. 133–134 (2000) 152–159, https://doi.org/10.1016/S0257-8972(00)00957-9.
[35] S. Vepřek, R.F. Zhang, M.G.J. Veprek-Heijman, S.H. Sheng, A.S. Argon, Superhard nanocomposites: Origin of hardness enhancement, properties and applications, Surf. Coat. Technol. 204 (2010) 1898–1906, https://doi.org/10.1016/J.SURFCOAT.2009.09.033.
[36] C.-L. Chang, C.-T. Lin, P.-C. Tsai, W.-Y. Ho, D.-Y. Wang, Influence of bias voltages on the structure and wear properties of TiSiN coating synthesized by cathodic arc plasma evaporation, Thin Solid Films 516 (2008) 5324–5329, https://doi.org/10.1016/j.tsf.2007.07.087.
[37] C.-L. Chang, C.-T. Lin, P.-C. Tsai, W.-Y. Ho, W.-J. Liu, D.-Y. Wang, Mechanical and corrosion properties of (Ti, Si) N coating synthesized by cathodic arc plasma evaporation, Surf. Coat. Technol. 202 (2008) 5516–5520, https://doi.org/10.1016/j.surfcoat.2008.06.029.
[38] Y. Moritz, C. Saringer, M. Tkadletz, A. Stark, N. Schell, I. Letofsky-Papst, C. Czettl, M. Pohler, N. Schalk, Oxidation behavior of arc evaporated TiSiN coatings investigated by in-situ synchrotron X-ray diffraction and HR-STEM, Surf. Coat. Technol. 404 (2020) 126632, https://doi.org/10.1016/j.surfcoat.2020.126632.
[39] S. Vepřek, M.G.J. Veprek-Heijman, P. Karvankova, J. Prochazka, Different approaches to superhard coatings and nanocomposites, Thin Solid Films 476 (2005) 1–29, https://doi.org/10.1016/J.TSF.2004.10.053.
[40] S. Vepřek, Conventional and new approaches towards the design of novel superhard materials, Surf. Coat. Technol. 97 (1997) 15–22, https://doi.org/10.1016/S0257-8972(97)00279-X.
[41] Y. Moritz, C. Kainz, M. Tkadletz, C. Czettl, M. Pohler, N. Schalk, Microstructure and mechanical properties of arc evaporated Ti(Al,Si)N coatings, Surf. Coat. Technol. 421 (2021) 127461, https://doi.org/10.1016/j.surfcoat.2021.127461.

[42] S. Zhang, D. Sun, Y. Fu, H. Du, Toughening of hard nanostructural thin films: a critical review, Surf. Coat. Technol. 198 (2005) 2–8, https://doi.org/10.1016/J.SURFCOAT.2004.10.020.
[43] J. Patscheider, Nanocomposite hard coatings for wear protection, MRS Bull. 28 (2003) 180–183, https://doi.org/10.1557/MRS2003.59.
[44] N. Schalk, M. Tkadletz, C. Mitterer, Hard coatings for cutting applications: Physical vs. chemical vapor deposition and future challenges for the coatings community, Surf. Coat. Technol. 429 (2022) 127949, https://doi.org/10.1016/J.SURFCOAT.2021.127949.
[45] F. Vaz, L. Rebouta, S. Ramos, M.F. Da Silva, J.C. Soares, Physical, structural and mechanical characterization of $Ti_{1-x}Si_xN_y$ films, Surf. Coat. Technol. 108–109 (1998) 236–240, https://doi.org/10.1016/S0257-8972(98)00620-3.
[46] F. Pei, Y.X. Xu, L. Chen, Y. Du, H.K. Zou, Structure, mechanical properties and thermal stability of $Ti_{1-x}Si_xN$ coatings, Ceram. Int. 44 (2018) 15503–15508, https://doi.org/10.1016/J.CERAMINT.2018.05.210.
[47] P.H. Mayrhofer, Structure/property relations in PVD hard coatings, in: Recent Res, Dev. Vac. Sci. Technol. (2003) 71–97.